Characteristics of a gold-doped electrode for application in high-performance lithium-sulfur battery

Vittorio Marangon[a,†], Daniele Di Lecce[b,c,†], Dan J. L. Brett[b,c], Paul R. Shearing[b,c,*], Jusef Hassoun[a,d,*]

[a] *University of Ferrara, Department of Chemical and Pharmaceutical Sciences, Via Fossato di Mortara 17, 44121, Ferrara, Italy*

[b] *Electrochemical Innovation Lab, Department of Chemical Engineering, UCL, London, WC1E 7JE, United Kingdom*

[c] *The Faraday Institution, Quad One, Becquerel Ave, Harwell Campus, Didcot OX11 0RA*

[d] *National Interuniversity Consortium of Materials Science and Technology (INSTM), University of Ferrara Research Unit, University of Ferrara, Via Fossato di Mortara, 17, 44121, Ferrara, Italy*

[*] Corresponding authors.

E-mail addresses: jusef.hassoun@unife.it (J. Hassoun), p.shearing@ucl.ac.uk (P.R. Shearing)

[†] These authors contributed equally to this work.

Keywords

Lithium-sulfur battery; Sulfur loading; Electrolyte/sulfur ratio; Gold nanoparticles; X-ray tomography

Abstract

Bulk sulfur incorporating 3 wt% gold nano-powder is investigated as possible candidate to maximize the fraction of active material in the Li-S battery cathode. The material is prepared via simple mixing of gold with molten sulfur at 120 °C, quenching at room temperature and grinding. Our comprehensive study reports relevant electrochemical data, advanced X-ray computed tomography (CT) imaging of the positive and negative electrodes, and a thorough structural and morphological characterization of the S:Au 97:3 *w*/*w* composite. This cathode exhibits high rate capability within the range from C/10 to 1C, with a maximum capacity above 1300 mAh g_S^{-1}, and capacity retention

between 85% and 91% after 100 cycles at 1C and C/3 rates. The novel formulation enables a sulfur fraction in the composite cathode film of 78 wt%, an active material loading of 5.7 mg cm^{-2}, and an electrolyte/sulfur (E/S) ratio of 5 μL $mg_{Ssulfur}^{-1}$, thus leading to a maximum areal capacity of 5.4 mAh cm^{-2}. X-ray CT at the micro- and nanoscale reveals the microstructural features of the positive electrode that favor fast conversion kinetics in the battery as well as the anode/electrolyte interphase. Quantitative analysis of sulfur distribution in the cathode displays that electrodeposition within the porous electrode during the initial cycle may trigger an activation process in the cell leading to the improved performance. Furthermore, the tomography study reveals the characteristic features of the lithium anode and the cell separator upon a galvanostatic test prolonged over 300 cycles at a 2C rate.

1. Introduction

Lithium sulfur (Li-S) batteries might enable a substantial breakthrough in energy storage technology [1] to accelerate the transition to sustainable electro-mobility [2–5]. The Li-S system overcomes the limits of gravimetric capacity of the insertion chemistry by exploiting the reversible conversion of sulfur to Li_2S, thereby delivering a theoretical energy density as high as 2600 Wh kg^{-1} (referred to the Li_2S mass) [6]. Moreover, the materials are intrinsically low-cost and with minimal environmental impact. Therefore, Li-S batteries are now receiving considerable attention from both the scientific community [7] and industry [8]. The last decade has been indeed characterized by noticeable advances in cell performance at the laboratory scale [6,9], while recent data on prototype batteries have suggested commercial viability in the near-term future [10]. In spite of these outstanding achievements, their launch into the market is currently hindered by challenges in cell design, mostly associated with the low electronic conductivity of elemental sulfur and Li_2S [11], as well as with the solubility of lithium polysulfide intermediates (Li_2S_x, $4 < x < 8$) in the electrolyte media [12,13]. The former issue may decrease the rate capability of the cell and limit the sulfur utilization, thus adversely affecting the practical capacity [11], whilst the latter may cause active material loss and poor cycle life by undesired reaction at the anode side of Li_2S_x species dissolved in the electrolyte [14]. Both issues have been partially addressed by engineering conductive carbon frameworks of various

morphologies [15–20] that can entrap sulfur and control its dissolution into the electrolyte [21]. On the other hand, parasitic reduction of polysulfides at the lithium-metal side can be effectively mitigated by adding a sacrificial agent to the electrolyte, e.g., $LiNO_3$, which is able to passivate the anode [22]. Cathode bulk conductivity is typically enhanced by incorporating a significant fraction of carbon in the active material formulation, although this may decrease the gravimetric energy density of the cell [11]. Moreover, carbon scaffolds may act as three-dimensional (3D) substrate for sulfur electrodeposition and Li_2S_2 or Li_2S precipitation, thereby supporting a large fraction of active material [23]. Following this trend, literature reports have demonstrated that the use of porous carbon cloths [24] and foams [25] instead of the typical Al current collector at the positive side of the cell may enhance the electrochemical performance in terms of reversible capacity and cycling stability [26,27], and increase the sulfur loading [28]. Notably, the E/S ratio significantly influences the complex mechanism that involves soluble Li_2S_x species, thereby controlling the behavior of the battery upon charge/discharge cycles and affecting the actual energy density [29]. Therefore, a great deal of effort from both academia and industry is now devoted to optimizing critical parameters being used in the cell configuration in order to achieve suitable values for technological applications, and fulfill the energy target of 500 Wh kg^{-1} [30]. In this regard, the development of innovative cathode designs is expected to play a crucial role in enabling practical batteries.

Recent studies have explored the possibility of including metal particles in the cathode film to enhance the charge transfer kinetics [31] and, possibly, catalyze the polysulfide conversion [32], by adapting an approach proposed earlier for lithium-ion [33,34] and lithium-oxygen [35] batteries. This strategy has the additional advantage of substantially decreasing the inactive materials in the electrode to boost the practical energy density of the cell [36]. Indeed, we have shown that high-performance cathode composites may be achieved by dispersing 15 wt% of Ni or Sn nanopowders in molten sulfur, thereby ensuring both high active material loading and low loading of additives in the positive electrode [36]. Furthermore, the incorporation of noble metal centers in the cathode has been indicated to favor the conversion reaction by possibly increasing the affinity of the electrode surface

toward lithium polysulfides and/or its bulk electronic conductivity [37–39]. Accordingly, X-ray photoelectron spectroscopy (XPS), and X-ray computed tomography (CT) analyses supported by electron microscopy have suggested favorable interactions between the metal site and polysulfides, promoting electrodeposition of sulfur on the porous cathode framework upon charging [36].

Bearing in mind these findings, we study herein the suitable characteristics of a gold-doped sulfur electrode for application in a lithium-sulfur battery. Notably, metal nanopowders benefit from a higher tap density than that of conventional carbon additives, which might be reflected as higher volumetric energy density in practical cells [31]. Hence, a scalable composite including 97 wt% of active material is prepared by melting sulfur in the presence of Au nanoparticles, which is comprehensively investigated via X-ray CT, electron microscopy, and X-ray diffraction (XRD). High-performance cathodes with a sulfur loading from ca. 2 to 6 mg cm^{-2} are coated on a porous carbon-based current collector and characterized in the lithium cell by combining various electrochemical techniques, including voltammetry, electrochemical impedance spectroscopy (EIS), and galvanostatic cycling. Furthermore, X-ray CT analyses at the microscale are used to shed light on the crucial role of cathode microstructure in enhancing sulfur conversion kinetics and cell performance.

2. Experimental

Elemental sulfur (≥99.5%, Riedel-de Haën) and gold nano-powder (<100 nm, 99.9% trace metal basis, Sigma-Aldrich) were mixed in the weight ratio of 97:3 and heated under magnetic stirring in a silicon oil bath at 120 °C until melting of sulfur and homogeneous blending of the two components was achieved. Subsequently, the mixture was cooled to room temperature and ground in an agate mortar after solidification. The resulting composite is indicated as S:Au 97:3 *w*/*w*. A further material with S:Au 85:15 *w*/*w* composition was prepared as above described.

The structure of the S:Au 97:3 *w*/*w* powder was investigated by means of XRD through a Bruker D8 Advance diffractometer equipped with a Cu-K_α source (8.05 keV) with a scan in the 2θ range between 10° and 90° at a rate of 10 s $step^{-1}$ with a step size of 0.02°. Morphology and elemental

composition of the S:Au 97:3 *w*/*w* powder were inspected by scanning electron microscopy (SEM), energy dispersive X-ray spectroscopy (EDS), transmission electron microcopy (TEM), and X-ray CT at the nanoscale. SEM-EDS was carried out through a Zeiss EVO MA10 using a tungsten thermionic electron source and equipped with an INCA X-ACT Oxford Instrument analyzer. TEM images were collected by a Zeiss EM 910 microscope employing a tungsten thermionic electron source operating at 100 kV. The X-ray CT analysis at the nanoscale was performed through a Zeiss Xradia 810 Ultra instrument (Carl Zeiss Inc.), employing a micro-focus rotating Cr anode (Cr-K_α of 5.4 keV, MicroMax-007HF, Rigaku). The X-ray source of the CT microscope was set at 35 kV and 25 mA. The specimen for X-ray nano-CT consisted of a small amount of powder S:Au 97:3 *w*/*w* secured on the tip of a stainless steel (SS) needle by epoxy [2,4,6-tris(dimethylaminomethyl)phenol, Devcon]. The X-ray nano-CT instrument comprises a He-filled chamber housing a condenser capillary that focused the beam onto the specimen and an He-filled optics chamber containing a Fresnel zone plate that focused the beam coming from the specimen onto a charge-coupled device (CCD) detector. A tomographic scan was carried out in absorption-contrast and large-field-of view (65 μm) mode by taking 901 radiographs of the sample through 180° rotation. Each radiograph was collected with an X-ray exposure time of 45 s and binning 1. The resulting voxel size was ca. 63 nm. The tomographic dataset was reconstructed through the Zeiss XMReconstructor software (Carl Zeiss Inc.) employing a filtered back-projection algorithm. The 3D reconstructed image was visualized, processed by applying nonlocal means and unsharp masking filters, and segmented through the Avizo 2019.4 software (Visualization Sciences Group, FEI SAS, Thermo Fisher Scientific). Three phases with increasing X-ray attenuation coefficient were identified by segmentation using grayscale [40] and watershed [41,42] methods: (i) exterior, (ii) sulfur, and (iii) gold.

S:Au 97:3 *w*/*w* electrodes were prepared by doctor-blade casting (MTI Corp.) a slurry containing the S:Au 97:3 *w*/*w* composite, conductive carbon black (Super P, Timcal), and polyvinilidene-fluoride (Solef® 6020 PVDF) in the weight ratio of 8:1:1, respectively. This slurry was prepared by dispersing the components in *N*-methyl-2-pyrrolidone (NMP, Sigma-Aldrich) by

means of an agate mortar and a pestle, and then cast on a carbon-cloth foil (GDL ELAT 1400, MTI Corp.). The wet electrode film was heated at 50 °C under air for about 3 h to evaporate the solvent. Cathode disks with a diameter of 14 mm (geometric area of 1.54 cm^2) were cut out from the dry coated foil, and then heated overnight at 40 °C under vacuum before being transferred in an Ar-filled glovebox (MBraun, O_2 and H_2O content below 1 ppm). Three batches of electrodes having different sulfur loading were prepared, that is, (i) in the range from 1.6 to 2.4 mg cm^{-2}, (ii) in the range from 4.1 to 5.7 mg cm^{-2}, and (iii) 1.4 mg cm^{-2}. Additional electrodes incorporating either S or S:Au 85:15 *w*/*w* and having a sulfur loading of about 2.4 mg cm^{-2} were prepared as above described.

CR2032 coin cells were assembled in an Ar-filled glovebox (MBraun, O_2 and H_2O content below 1 ppm) by stacking a lithium disk with diameter of 14 mm, a Celgard 2400 separator with diameter of 16 mm soaked by the electrolyte solution, and a S:Au 97:3 *w*/*w* electrode. The electrolyte solution was obtained by dissolving lithium bis(trifluoromethanesulfonyl)imide (LiTFSI, 99.95% trace metals basis, Sigma-Aldrich) and lithium nitrate ($LiNO_3$, 99.99% trace metals basis, Sigma-Aldrich) in a mixture of 1,3-dioxolane (DOL, anhydrous, contains ca. 75 ppm BHT as inhibitor, 99.8%, Sigma-Aldrich) and 1,2-dimethoxyethane (DME, anhydrous, 99.5%, inhibitor-free, Sigma-Aldrich) in the 1:1 *w*/*w* ratio. Prior to use, LiTFSI and $LiNO_3$ were dried at 110 and 80 °C, respectively, under vacuum for 3 days, while DOL and DME were dried under molecular sieves (3 Å, rod, size 1/16 in., Honeywell Fluka) until the water content was lower than 10 ppm, as measured by a Karl Fischer 899 Coulometer (Metrohm). The final concentration of each salt in the electrolyte solution was 1 mol kg^{-1} as referred to the weight of solvent.

Cyclic voltammetry (CV) measurements were carried out at a scan rate of 0.1 mV s^{-1} in the 1.8–2.8 V vs. Li^+/Li potential range. Electrochemical impedance spectra were collected at the open circuit voltage (OCV) condition of the cell, as well as after 1, 5 and 10 CV cycles, and analyzed through the non-linear least squares (NLLS) fitting method via the Boukamp software (χ^2 values of the order of 10^{-5}) [43,44]. EIS was performed by applying to the cell an alternate voltage signal with amplitude of 10 mV within the frequency range from 500 kHz to 100 mHz. Further CV scans in the

1.8–2.8 V vs. Li^+/Li potential range at increasing scan rates, i.e., 0.05, 0.1, 0.15, 0.2 and 0.25 mV s^{-1}, were performed to estimate the apparent Li^+ diffusion coefficients (D) according to the Randles-Sevcik equation [45,46]:

$$I_p = 0.4463zFAC\left(\frac{zFvD}{RT}\right)^{\frac{1}{2}} \quad (1)$$

where I_p is the peak current (A), z is the number of exchanged electrons, F is the Faraday constant (96 485 C mol^{-1}), A is the geometric area of the S:Au 97:3 *w*/*w* electrode (1.54 cm^2), C is the estimated Li^+ concentration in the electrode volume (mol cm^{-3}), v is the scan rate (mV s^{-1}), D is the Li^+ diffusion coefficient (cm^2 s^{-1}), R is the gas constant (8.31451 J mol^{-1} K^{-1}) and T is the room temperature (298 K). Herein, a number of 1 exchanged electron (z = 1) was considered for each discharge peak (occurring at about 2.3 and 2.0 V), whilst a number of 2 exchanged electrons (z = 2) was taken into account for the charge peak (occurring at about 2.4 V). The CV and EIS measurements were performed through a VersaSTAT MC Princeton Applied Research (PAR) analyzer.

Galvanostatic cycling (GC) measurements were carried using a MACCOR series 4000 battery test system. Coin cells with a S loading between 1.9 and 2.2 mg cm^{-2} over the electrode and an electrolyte/sulfur (E/S) ratio of 15 µL mg_{Sulfur}^{-1} were tested within the current rate ranging from 1C to C/10 (1C = 1675 mA g_S^{-1}). In detail, galvanostatic measurements over 100 cycles were carried out at C/3 and 1C rates within the 1.9–2.8 V and 1.8–2.8 V voltage ranges, respectively. The rate capability of the electrode was assessed by applying current rates of C/10, C/8, C/5, C/3, C/2 and 1C, increasing every 5 cycles and decreasing to the initial value of C/10 at the 26th cycle. Voltage ranges of 1.9–2.8 V from C/10 to C/2 and of 1.8–2.8 V at 1C were set for this rate capability test. Coin cells with a S loading of 5.7 mg cm^{-2} and an E/S ratio of 5 µL mg_{Sulfur}^{-1} were cycled at a constant current rate of C/20 rate between 1.8 and 2.8 V. A further Li|S:Au 97:3 *w*/*w* coin cells with a sulfur loading over the electrode of 1.4 mg cm^{-2} and an E/S ratio of 15 µL $mg_{Sulfur}^{-1}$was subjected to prolonged cycling at the 2C rate between 1.8 and 2.8 V.

The effect of gold incorporation on the electrochemical properties of the sulfur cathode was further evaluated by measuring the sheet resistance, the Warburg resistance, and the maximum capacity in lithium cell of materials prepared by using bulk sulfur without any metal additive, and composites containing Au nanoparticles with weight ratio of 3% (S:Au 97:3 *w*/*w*) and 15 % (S:Au 85:15 *w*/*w*). The sheet electrical resistance was determined by 4-point probe measurements (Jandel RM3000+ Test Unit) on pellets incorporating 90 wt% cathode material and 10 wt% carbon black, where the cathode material is bulk S, S:Au 97:3, or S:Au 85:15, respectively. The Warburg resistance was measured by EIS on lithium cells using pelletized cathodes prepared by pressing S, S:Au 97:3 *w*/*w*, or S:Au 85:15 *w*/*w*. Thin films of S and S:Au 85:15 *w*/*w* formed by 80 wt% cathode material, 10 wt% polymer binder, and 10 wt% carbon black, with S loading of about 2.4 mg cm^{-2} and an E/S ratio of 15 μL mg_{Sulfur}^{-1}, were also tested in lithium cells as control samples by galvanostatic cycling at the constant current rate of C/3 as described above.

The S:Au 97:3 *w*/*w* electrode, the lithium-metal anode, and the separator were imaged before and after cycling in the lithium cell by X-ray CT at the microscale using a Zeiss Xradia 620 Versa microscope (Carl Zeis Inc.) employing a polychromatic microfocus source (tungsten target). Cathode samples for X-ray micro-CT were prepared by cutting out portions with approximate size of 1 mm × 1 mm form each electrode and securing these to SS dowels by epoxy [2,4,6-tris(dimethylaminomethyl)phenol, Devcon]. Tomographic scans of the cathodes were performed using a 40× lens and collecting 1601 radiographs of the specimen through 360° rotation with binning 1. Voltage and current of the X-ray source, time of exposure for each projection, as well as source–specimen and detector–specimen distances, were adjusted to obtain suitable transmission values. In detail, electrodes with a sulfur loading from 1.6 to 2.4 mg cm^{-2} were investigated setting the source in the 80–90 kV and 87–89 μA ranges, whilst electrodes with a sulfur loading from 4.1 to 4.2 mg cm^{-2} were studied setting the source at 120 kV and 83 μA. The exposure time varied from 44 to 47 s, whilst the source–specimen and detector–specimen distances were in the ranges of 9.77–9.81 and 8.95–9.05 mm, respectively, thereby leading to a voxel size between 176 and 177 nm in a field of

view of about 330 μm. The anode and separator samples were recovered from two Li|S:Au 97:3 *w*/*w* coin-cells, which were held at OCV and discharged/charged at a 2C rate upon 300 cycles, respectively (1C = 1675 mAh g_S^{-1}). Both cells had a sulfur loading over the electrode of 1.4 mg cm^{-2} and an E/S ratio of 15 μL mg_{Sulfur}^{-1}. Cell disassembling was carried out in an Ar-filled glovebox (MBraun, O_2 and H_2O content below 1 ppm). Afterwards, lithium and separator samples were cut out and sealed inside Swagelok-type cells having polyether ether ketone (PEEK) housing and stainless steel (SS) pins, which had an inner diameter of 0.8 mm, in order to avoid air exposure during the X-ray CT scans. These scans were performed by collecting 901 radiographs of the specimen through 360° rotation and using a 20× lens and binning 1. The source was set at 60 kV and 83 μA, the exposure time was 30 s, and source–specimen and detector–specimen distances were adjusted to obtain suitable transmission values and a voxel size of 301 nm. The micro-CT datasets were reconstructed through the Scout-and-Scan Control System Reconstructor software (Carl Zeiss Inc.) employing either a filtered back-projection algorithm (cathode) or the Optirecon algorithm (anode and separator). The 3D reconstructed images were visualized, processed by applying nonlocal means and unsharp masking filters, segmented, and quantitatively analyzed through the 2020.2 software (Visualization Sciences Group, FEI SAS, Thermo Fisher Scientific). Four domains with increasing X-ray attenuation coefficient were identified in the cathode by segmentation using grayscale [40] and watershed [41,42] methods: (i) exterior, (ii) a domain including carbon, PVDF and carbon-cloth support, (iii) sulfur, and (iv) gold. For cathode analysis, binary datasets were produced by selecting the segmented sulfur domain, and the phase fraction of sulfur along the *Z* axis, i.e., the specimen rotation axis orthogonal to the electrode plane, was calculated. Electrodes used for X-ray CT with a sulfur loading from 1.6 to 2.4 mg cm^{-2} were cycled at a 1C rate, whilst the those with a sulfur loading from 4.1 to 4.2 mg cm^{-2} were cycled at a C/10 rate.

3. Results and discussion

The composite cathode material has been prepared by mixing molten sulfur and gold particles in the weight ratio of 97:3, according to a straightforward approach recently reported [31,36]. Figure 1

shows the structural and morphological characteristics of the S:Au 97:3 *w*/*w* powder as studied by combining XRD, electron microscopy, and X-ray CT techniques. XRD reveals the patterns of orthorhombic sulfur (α-S_8) and metallic gold, with relative peak intensities reflecting the volume ratio between the two phases and suggesting large crystal domains for sulfur (Fig. 1a). The absence of reflections attributed to additional phases confirms that the mild conditions adopted to make the composite, along with the well-known inert nature of metallic gold [47], actually prevent the formation of impurities or side products. SEM images at various magnifications (Fig. 1b, c and g) and EDS maps (Fig. 1f and h) display sub-micrometric Au agglomerates laying on sulfur particles with a size from about 5 μm to about 50 μm, as well as segregated larger Au clusters with maximum size approaching 30 μm. Each metal aggregate is mostly formed by nanometric primary particles below 100 nm, as evidenced by the TEM image in Fig. 1(i). X-ray CT at the nanoscale enables a three-dimensional reconstruction of a portion of the composite of about 60 μm. The related cross-sectional slice with corresponding three-phase segmentation (Fig. 1d and e) and the volume rendering (Fig. 1j) reveal a large sulfur cluster with irregular shape containing few Au domains below 1 μm. It is worth noting that the dispersion of a low fraction of noble metal into a bulk of active material evidenced in Fig. 1 may actually lead to an increased energy density of the electrode, and mitigate the insulating character of sulfur to boost the conversion in lithium cell [31]. Indeed, gold is expected to enhance the reaction kinetics at the electrode/electrolyte interphase and favor the electrodeposition of sulfur and possibly the formation of Li_2S [36].

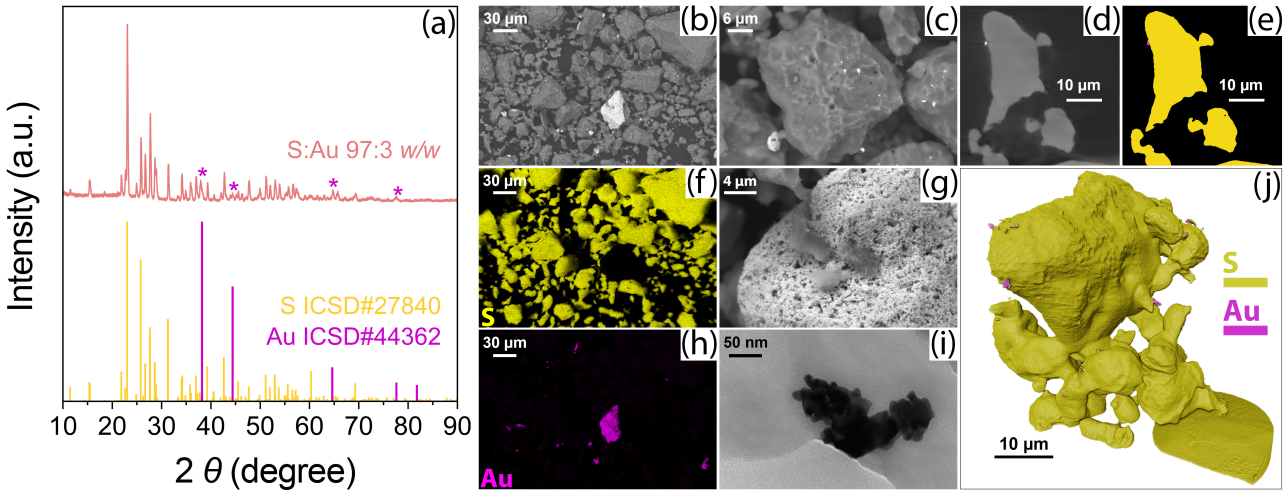

Fig. 1. (a) XRD pattern of the S:Au 97:3 *w/w* powder (top) and reference data (bottom) for elemental sulfur (yellow, ICSD #27840) and metallic gold (magenta, ICSD #44362). (b–j) Morphological analysis of the S:Au 97:3 *w/w* powder by electron microscopy and X-ray CT. In detail: (b, c and g) SEM images at various magnifications in (b and c) backscattered and (g) secondary electron modes; (f, h) EDS maps of (f) S and (h) Au; (i) TEM image; (d, e and j) X-ray CT imaging at the nanoscale, as (d) cross-sectional slice extracted in a plane along the rotation axis (beam attenuation represented through a grayscale), (e) corresponding three-phase segmented slice (Au: magenta, S: yellow, exterior: black), and (j) three-phase segmented volume rendering (Au: magenta, S: yellow, exterior: not represented); tomographic scan performed in absorption-contrast, large-field-of view (65 µm) mode by taking 901 radiographs of the specimen through 180° with an exposure time of 45 s for each projection and binning 1; voxel size of reconstructed CT datasets: 63 nm.

The electrochemical process of the S:Au 97:3 *w/w* cathode in the cell has been characterized by voltammetry and impedance spectroscopy measurements (Fig. 2). The first reduction scan of Fig. 2(a) reveals two peaks at about 2.20 and 2.00 V vs. Li^+/Li, which can be associated with the formation of long-chain and short-chain lithium polysulfides, i.e., Li_2S_x with $6 \leq x \leq 8$ and $2 \leq x \leq 4$, and possibly Li_2S [12,48,49]. The subsequent oxidation scan is instead characterized by a broad double peak with maximum centered at 2.35 and 2.40 V vs. Li^+/Li, reflecting the reversible reaction of Li_2S_x species ($1 \leq x \leq 8$) with final electrodeposition of S_8 at high potential [12,49]. After the initial cycle, Fig. 2(a) shows a notable shift of the first discharge peak from 2.20 V vs. Li^+/Li to 2.30 V vs. Li^+/Li, and a slight decrease in polarization for the second discharge peak. This electrochemical behavior suggests an improvement of the charge transfer at electrode/electrolyte interphase along with microstructural

rearrangements in the cathode upon multiphase conversion of sulfur, in good agreement with earlier reports [36,50,51]. These modifications lead also to an additional shoulder in the potential range of 2.5–2.7 V vs. Li^+/Li during the oxidation scans, thus suggesting a change in the conversion kinetics. This phenomenon likely involves sulfur precipitation during charge on preferred locations over the electrode [36,51] which generally leads to an electrochemical activation, and increases the active material utilization via activation of suitable reaction sites on the cathode surface [36]. This hypothesis is in part supported by the different signature of the first CV scan compared to the overlapping profiles of the subsequent cycles (Fig. 2a). Furthermore, EIS indicates a significant drop in electrode/electrolyte interphase resistance (R_i) after the first scan and a steady response for the subsequent 10 cycles (see the related Nyquist plot in Fig. 2b). Table 1 reports the results of an NLLS fitting of the impedance data performed by modeling the cell response with the $R_e(R_iQ_i)_nQ_g$ equivalent circuit (n = 1, 2), where the high-middle frequency sub-circuit containing pseudo-capacitive and resistive elements arranged in parallel [i.e., $(R_iQ_i)_n$] reproduces the electrode/electrolyte interphase, whilst R_e and Q_g simulate the electrolyte resistance and the cell capacitance, respectively [43,44,52]. This analysis suggests a decrease in R_i from 216 ± 1 Ω at the OCV condition (inset of Fig. 2b) to values fluctuating between 3.4 ± 0.3 Ω and 4.0 ± 0.2 Ω during the subsequent cycles (main panel of Fig. 2b), and reflects a remarkable improvement of the charge transfer kinetics due to the above mentioned activation [36,50].

Table 1. Results of NLLS analysis [43,44] of impedance spectra of the Li|S:Au 97:3 *w*/*w* cell collected upon a CV measurement. In detail: cell condition; equivalent circuit; electrode/electrolyte interphase resistances ($R_{i,1}$, $R_{i,2}$, R_i); χ^2 parameter. EIS carried out by applying to the cell an alternate voltage signal with amplitude of 10 mV within the frequency range from 500 kHz to 100 mHz. See Fig. 2(a and b) showing the related CV profiles and Nyquist plots. Electrode geometric area: 1.54 cm^2. Electrolyte: 1 mol kg^{-1} LiTFSI, 1 mol kg^{-1} $LiNO_3$ in DOL:DME 1:1 *w*/*w*. Temperature: 25 °C.

Cell condition	Equivalent circuit	$R_{i,1}$ (Ω)	$R_{i,2}$ (Ω)	R_i ($R_{i,1}$ + $R_{i,2}$) (Ω)	χ^2
OCV	$R_e(R_{i,1}Q_1)Q_g$	216 ± 1	/	216 ± 1	8×10^{-5}
After 1 CV cycle	$R_e(R_{i,1}Q_1)(R_{i,2}Q_2)Q_g$	2.1 ± 0.1	1.9 ± 0.2	4.0 ± 0.2	8×10^{-5}
After 5 CV cycles	$R_e(R_{i,1}Q_1)(R_{i,2}Q_2)Q_g$	2.4 ± 0.1	1.0 ± 0.3	3.4 ± 0.3	2×10^{-5}
After 10 CV cycles	$R_e(R_{i,1}Q_1)(R_{i,2}Q_2)Q_g$	2.8 ± 0.1	0.8 ± 0.2	3.6 ± 0.2	3×10^{-5}

CV scans at various scan rates have been carried out to estimate the apparent Li^+ diffusion coefficient (*D*) by applying the Randles-Sevcik equation (1) [15,45,46,53]. The related voltammetry profiles, shown in top panel of Fig. 2c, display the expected raise in polarization and peak current intensity as the scan rate increases from 0.05 to 0.25 mV s^{-1}, along with the appearance of the abovementioned additional shoulder during charging from 2.6 to 2.7 V vs. Li^+/Li. Notably, the linear relation between the I_p and the square root of the scan rate ($v^{1/2}$) evidenced by Fig. 2(d) suggests an electrochemical process limited by diffusion, despite the substantial difference between the Randles-Sevcik system [45,46] and the cell herein investigated [36] (see linear fitting parameters in Figure S1 and Table S1 of the Supplementary Material). Therefore, a *D* value is calculated for each reduction peak as well as for the double oxidation peak according to previous reports, and reported in Table 2 and in the bottom panel of Fig. 2(c) [15,36,53,54]. The apparent diffusion coefficient ranges between 7.8×10^{-8} and 1.1×10^{-7} cm^2 s^{-1} at the various states of charge of the cell (Table 2) and decreases at the end of discharge, thus in agreement with the extensively described reaction kinetics which hinders the final steps of sulfur conversion to short-chain lithium polysulfides and possibly to Li_2S [24]. An additional slight decrease of *D* during charging reflects the partially limited ion diffusion into the

insulating sulfur electrodeposited over the electrode, which may actually be improved by providing proper electrodeposition sites in order to allow a reversible electrochemical process at high current rates [55,56]. In this regard, the dispersion of metal nanoparticles within the cathode has proven to be an effective strategy to enhance the multiphase conversion reactions [31,36]. Herein, we have further improved this approach by exploiting the highly conductive gold nano-powder, which has enabled satisfactory electrode kinetics despite an inactive metal amount as low as 3%, thus leading to a final sulfur ratio into the cathode film of 78 wt% and, possibly, high energy density.

Table 2. Li^+ diffusion coefficient (D) calculated by applying the Randles-Sevcik equation to CV data (Equation (1) in the Experimental section) [45,46]. Fig. 2(c) displays the corresponding CV profiles in the 1.8–2.8 V vs. Li^+/Li potential range (upper panel) at various scan rates, that is, 0.05, 0.1, 0.15, 0.2 and 0.25 mV s^{-1}, and the D coefficients (bottom panel). Fig. 2(d) shows the corresponding peak current trends; the related linear fittings parameters are reported in Fig. S1 and Table S1.

State of charge	D (cm^2 s^{-1})
2.30 V vs. Li^+/Li (disch.)	1.1×10^{-7}
1.95 vs. Li^+/Li (disch.)	9.6×10^{-8}
2.35 V vs. Li^+/Li (ch.)	7.8×10^{-8}

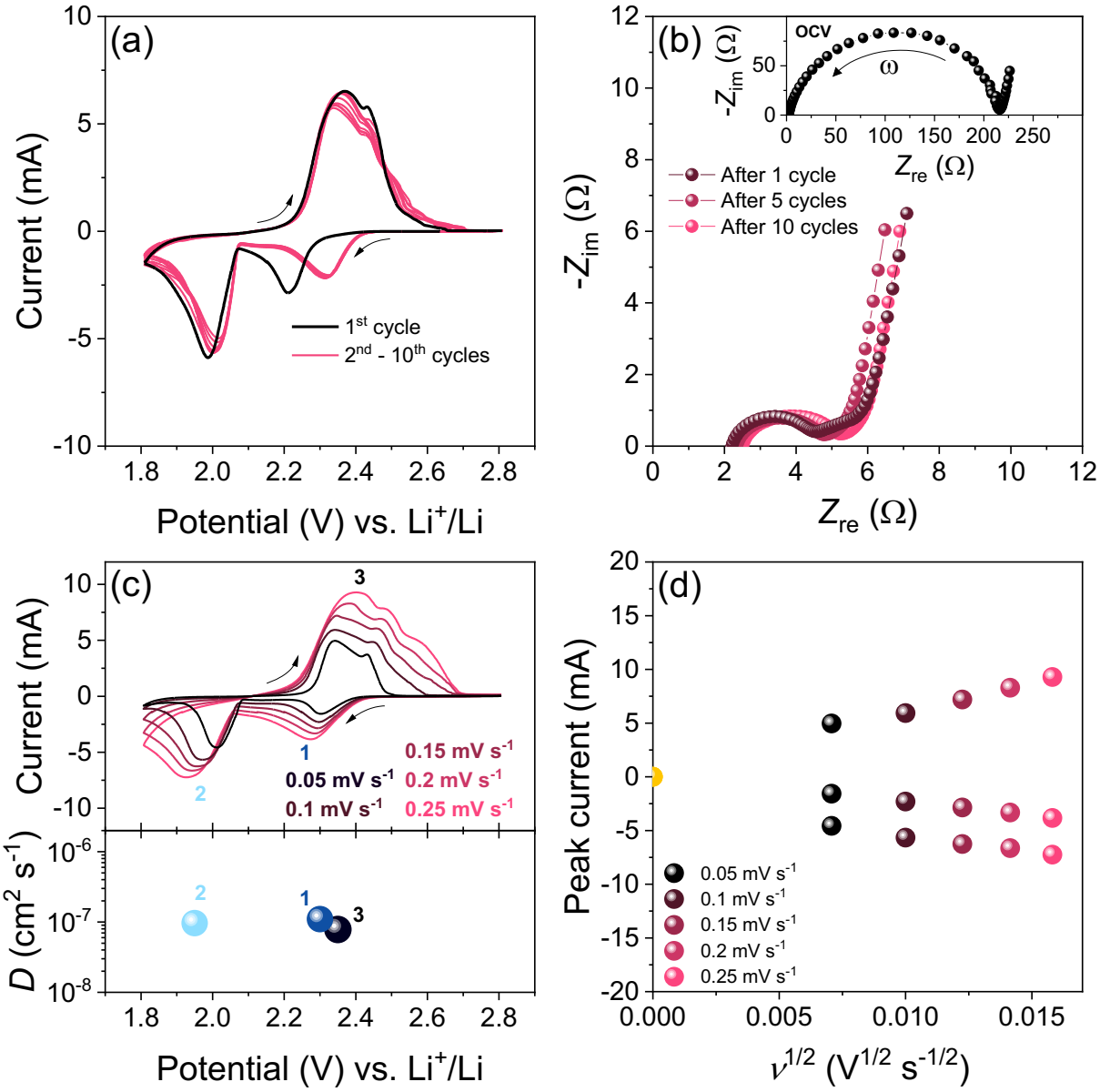

Fig. 2. (a) CV profiles of the Li|S:Au 97:3 *w*/*w* cell at a scan rate of 0.1 mV s^{-1} within the potential range from 1.8 to 2.8 V vs. Li^+/Li and (b) Nyquist plot of impedance spectra of the same cell at the OCV and after 1, 5 and 10 voltammetry cycles; EIS carried out by applying to the cell an alternate voltage signal with amplitude of 10 mV within the frequency range from 500 kHz to 100 mHz. (c) CV profiles (upper panel) of the Li|S:Au 97:3 *w*/*w* cell at various scan rates, i.e., 0.05, 0.1, 0.15, 0.2 and 0.25 mV s^{-1} within the potential range from 1.8 to 2.8 V vs. Li^+/Li and apparent Li^+ diffusion coefficient (*D*, bottom panel) calculated by applying the Randles-Sevcik equation to the CV data (see Equation (1) in the Experimental section and Table 2). (d) Peak current as a function of the square root of the scan rate ($v^{1/2}$) extracted from the CV profiles of panel (c); the yellow point indicates the axes origin; see Fig. S1 and Table S1 in the Supplementary Material for the corresponding linear fitting parameters. Electrode geometric area: 1.54 cm^2. Electrolyte: 1 mol kg^{-1} LiTFSI, 1 mol kg^{-1} $LiNO_3$ in DOL:DME 1:1 *w*/*w*. Temperature: 25 °C.

Fig. 3 reports the features in lithium cells of the S:Au 97:3 *w*/*w* electrode by exploiting an average sulfur loading typically used for Li-S battery study (i.e., of about 2 mg cm^{-2}). The cells are galvanostatically cycled at various currents in order to verify the rate capability of the electrode (Fig. 3a and d), as well as at a constant rate of C/3 (Fig. 3b and e) and 1C (Fig. 3c and f) to evaluate the cycle life. In detail, the battery reveals suitable response characterized by a moderate increase in polarization (Fig. 3a) and a limited decrease in capacity by gradually raising the C-rate from C/10 to 1C (Fig. 3d). The voltage profiles at C/10 show two plateaus centered at about 2.35 and 2.10 V during discharge, and at 2.40 and 2.20 V during charge (Fig. 3a), in agreement with the CV curves already shown in Fig. 2. In spite of the abovementioned overvoltage increase by incremental raise in the C-rate, the cell almost fully restores its maximum capacity as the current is lowered back to the initial value of C/10 at the end of the test. Indeed, Fig. 3d shows capacity values of about 1314, 1237, 1156, 1039 and 890 mAh g_S^{-1} at the rates of C/10, C/8, C/5, C/3 and 1C, respectively, as well as a capacity of 1260 mAh g_S^{-1} when the current is lowered back to C/10 after 25th cycle which reflects a 96% of retention. Additionally, galvanostatic tests prolonged over 100 cycles at the constant current rates of C/3 (Fig. 3b and e) and 1C (Fig. 3c and f) evidence excellent performance. Both tests show an activation occurring upon the initial 10–15 cycles which leads to a progressive improvement of the voltage profile to a steady-state characterized by lower polarization (Fig. 3b and c). Furthermore, this ongoing process leads to a steep increase in the delivered capacity from about 800 mAh g_S^{-1} at C/3 and 600 mAh g_S^{-1} at 1C to values approaching 1200 and 1000 mAh g_S^{-1}, respectively (Fig. 3e and f). After 100 cycles, the battery retains 940 mAh g_S^{-1} at C/3 and 910 mAh g_S^{-1} at 1C, which corresponds to ca. 85% and 91% of the steady-state values. Notably, the data of Fig. 3 show a coulombic efficiency approaching 100% upon the first cycle and suggest an effectual mitigation of possible parasitic reactions of the dissolved polysulfides due to the *in situ* protection of the lithium anode by using a suitable electrolyte solution [57]. It is worth mentioning that cell configuration in terms of composition and microstructure of the cathode, electrolyte formulation, and E/S ratio may significantly affect the electrochemical performance [30]. Accordingly, the Li|S:Au 97:3 *w*/*w* cell

actually benefits from a cathode optimized by gold-doping [31,36], a porous support with suitable sulfur electrodeposition sites [26,27], an electrolyte solution containing $LiNO_3$ to avoid the "shuttle effect" and massive formation of dendritic structures [57,58], and an E/S ratio of 15 μL mg_{Sulfur}^{-1}.

Literature studies [31,32] have shown that the inclusion of metal nanoparticles in the electrode may catalyze the polysulfide conversion and enhance the charge transfer kinetics. On the other hand, we reasonably supposed that gold incorporation mainly increases the electrical conductivity of the cathode, thereby mitigating the insulating character of sulfur, although minor catalytic effects on the polysulfide reaction mechanism cannot be excluded [32]. In order to verify this hypothesis, we have performed 4-point probe measurements on pelletized electrode samples, and compared the electrochemical performance of thin-film cathodes incorporating bulk sulfur as well as composites with a weight ratio of gold nanoparticles of 3% and 15%, respectively. The related results are reported in Table 3 and in Fig. S2(a and c) of the Supplementary Material (see the Experimental section for further details on the measurements). As expected, the data of Table 3 reveal the raise in electrical conductivity caused by the addition of gold in the pellet, which leads to an increase in maximum reversible capacity. Notably, both conductivity and maximum capacity appear to be in a relation of proportionality with the Au content (Table 3 and Fig. S2a and c), while the effect of gold concentration in the cathode on the cycling trend is not straightforward (Fig. S2b). This trend possibly suggests a complex interplay between sulfur utilization and active material loss during the initial stages of the electrochemical test. On the other hand, EIS measurements on Li-S cells using material pellets (Fig. S2d–f in the Supplementary Material, with pellets shown in inset) suggest that the presence of Au has further beneficial effects in decreasing the Warburg resistance of the electrode to the Li^+ transport (Table 3). Computational modelling by first-principles density functional theory (DFT) calculations might possibly provide further insight on the absorption of lithium polysulfides over functionalized surfaces and reveal electrocatalytic effects on the Li-S conversion reaction [59,60].

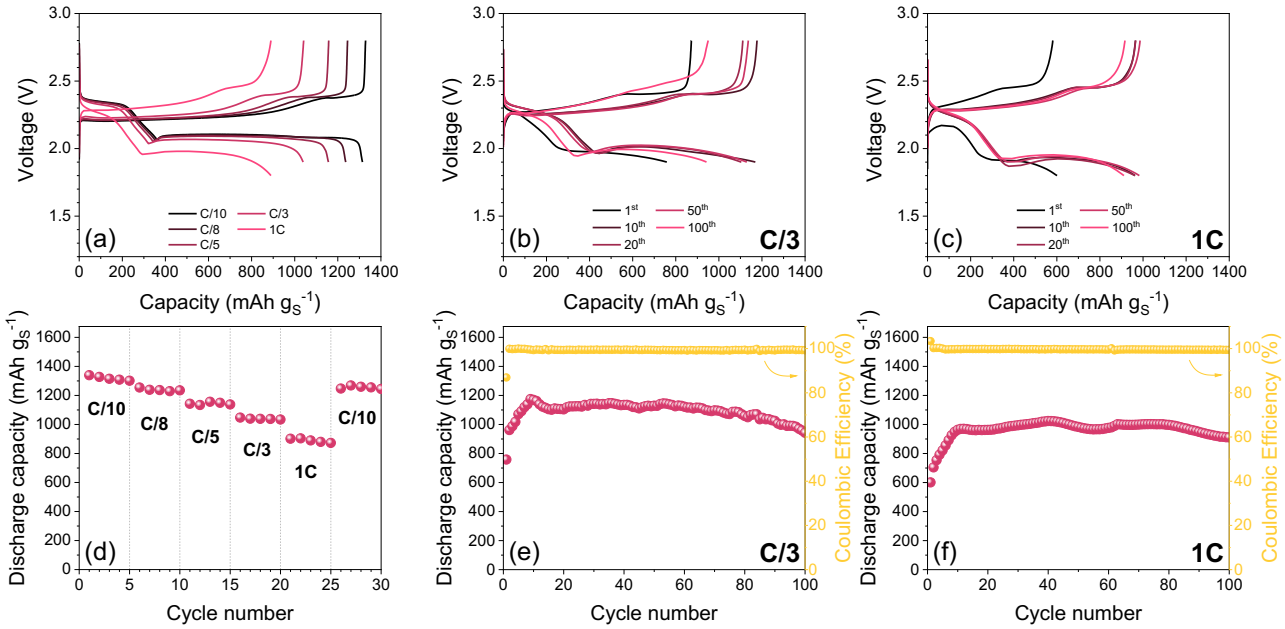

Fig. 3. (a–c) Voltage profiles and (d–f) cycling trends in various testing conditions of the Li|S:Au 97:3 *w*/*w* cell with sulfur loading over the electrode of 1.9–2.2 mg cm^{-2} and E/S ratio of 15 µL mg$_{Sulfur}^{-1}$. In detail: (a and d) rate capability of the cell within the range from C/10 to 1C, namely, at C/10, C/8, C/5, C/3 and 1C (1C = 1675 mA g$_S^{-1}$); (b, c, e and f) performance of the cell over 100 cycles at constant current rates of (b and e) C/3 and (c and f) 1C. Voltage ranges: 1.9–2.8 V from C/10 to C/3 rate and 1.8–2.8 at 1C rate. Electrode geometric area: 1.54 cm^2. Electrolyte: 1 mol kg^{-1} LiTFSI, 1 mol kg^{-1} $LiNO_3$ in DOL:DME 1:1 *w*/*w*. Temperature: 25 °C.

Table 3. Effect of gold on the electrochemical properties of the sulfur cathode. In detail: sheet electrical resistance as determined by 4-point probe measurements on pellets incorporating 90 wt% cathode material and 10 wt% carbon black, where the cathode material is either bare S, or S:Au 97:3 *w*/*w*, S:Au 85:15 *w*/*w*; Warburg resistance as measured by EIS on lithium cells using pelletized cathodes prepared by pressing either S, or S:Au 97:3 *w*/*w*, S:Au 85:15 *w*/*w*; maximum discharge capacity in lithium cells at the constant current rate of C/3 for thin film electrodes with 80 wt% cathode material, 10 wt% polymer binder, 10 wt% carbon black (1C = 1675 mA g$_S^{-1}$), where the cathode material is either S, or S:Au 97:3 *w*/*w*, S:Au 85:15 *w*/*w*, and the sulfur loading over the electrode and the E/S ratio are of about 2.4 mg cm^{-2} and 15 µL mg$_{Sulfur}^{-1}$, respectively. See Fig. S2 for corresponding experiments.

Material	Sheet resistance (Ω/□)	Warburg resistance (Ω)	Discharge capacity (mAh g$_S^{-1}$)
S	56.6 ± 0.9	25.1 ± 0.5	920 ± 90
S:Au 97:3 *w*/*w*	34.8 ± 0.8	24.2 ± 0.5	1000 ± 100
S:Au 85:15 *w*/*w*	25.2 ± 0.7	15.1 ± 0.6	1200 ± 100

The effects of cycling on the cathode microstructure are subsequently investigated by performing X-ray CT scans in a field of view of about 330 μm (Fig. 4). These measurements provide a three-dimensional map of the various phases in the electrode which are identified by differences in X-ray attenuation, thus enabling the detection of morphological features at the microscale with a voxel size smaller than 180 nm. Fig. 4 shows the X-ray imaging of cathode samples before (panels a–c) and after 1 (panels d–f) and 100 cycles (panels g–i). The left-hand side panels (Fig. 4a, d and g) report sections of the electrodes represented in grayscale, where the brightness reflects the local density of the specimen [40]. Accordingly, the large Au aggregates already observed in detail by SEM-EDS, TEM, and X-ray CT at the nanoscale in Fig. 1, can be detected as continuous bright spots in Fig. 4 a, d and g, whilst sulfur appears as gray particles with moderate density [36,42]. However, it is worth mentioning that smaller gold nanoparticles intimately mixed with sulfur cannot be detected by microscale CT [36]. Besides, X-ray imaging reveals that the carbon-cloth support and the carbon-binder domain of the composite electrode film have lower density than sulfur, as suggested by the brightness scale of the images [36,42]. Four domains are identified by analyzing the grayscale histogram of the CT reconstructions [40], and image segmentation is performed by processing the 3D datasets as described in the Experimental section. Fig. 4(b, e and h) show the segmented images of the electrode and depict (i) highly attenuating gold in magenta, (ii) moderately attenuating sulfur in yellow, (iii) lowly attenuating carbon cloth and carbon-binder domain in gray, and (iv) exterior/pores in black. Furthermore, of Fig. 4(c, f and i) display volume of the electrode domains using the same color map. Additional imaging of the electrodes is given by supplementary animations obtained by X-ray CT tomography (Movies S1).

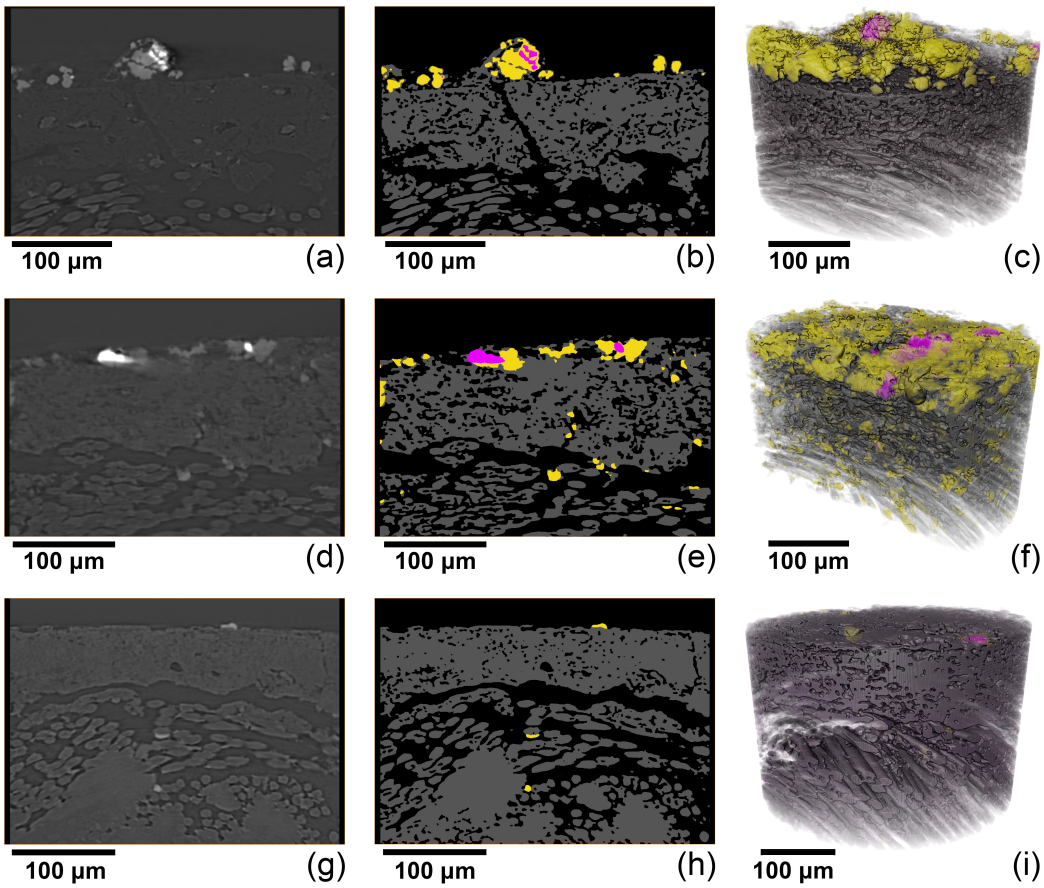

Fig. 4. X-ray CT imaging at the microscale of S:Au 97:3 *w*/*w* electrodes with sulfur loading of 1.6–2.4 mg cm^{-2} (a–c) before and after (d–f) 1 and (g–i) 100 cycles at a 1C rate. In detail: (a, d and g) cross-sectional slices extracted in a plane parallel to the rotation axis (*Z* axis) and orthogonal to the electrode plane (beam attenuation represented through a grayscale), (b, e, h) corresponding four-phase segmented slices (Au: magenta, S: yellow, C/PVDF/C-cloth: gray; exterior: black), and (c, f and i) four-phase segmented volume rendering (Au: magenta, S: yellow, C/PVDF/C-cloth: gray; exterior: not represented). Tomographic scans performed using a 40× lens and taking 1601 radiographs of the specimen through 360° with an exposure time of either 44 or 47 s for each projection and binning 1; voxel size: from 176 nm to 177 nm: field of view: ~ 330 µm. See Figures 3 and 5 showing the cycling performance of the cell and the distribution of the sulfur phase in the electrode samples, respectively.

In agreement with earlier reports [36,61], the tomographic datasets of Fig. 4a–f suggest that the electrochemical activation of the cell is associated with a substantial reorganization of sulfur particles randomly distributed in the pristine cathode film, which dissolve during discharge and precipitate on suitable sites over the electrode surface during charge. Indeed, the multi-phase nature of the conversion process in the cell may enable favorable microstructural rearrangements in the electrode leading to an actual enhancement of the charge transfer kinetics at the interphase with the electrolyte solution [36]. Therefore, improved performances may be achieved by tailoring preferred electrodeposition sites for sulfur and suitable hosts for Li_2S on the cathode, as well as by using a porous current collector which may accommodate the active material [26,36]. On the other hand, we have recently observed that the pristine electrode morphology may affect the cell behavior possibly altering the nucleation rate of the solid species at the cathode side, the sulfur utilization, and the active material loss over long-term cycling [42]. Fig. 4(g–i) evidence a significant decrease in volume fraction of sulfur in the electrode after 100 cycles, which can be only in part related to the capacity fade observed in Fig. 3. Indeed, the data of Fig. 4 suggest a certain role played by the lithium polysulfides dissolved into the electrolyte as a catholyte in boosting the electrochemical process of the cell and ensuring a satisfactory performance [28].

Fig. 5 reports a quantitative analysis of sulfur distribution within the instrumental field of view as determined by processing the tomographic data of the electrodes before (panels a and b) and after 1 (panels c and d) and 100 cycles (panels e and f) in Li-S cell. The volume renderings of the sulfur phase across a plane orthogonal to the electrode are represented in Fig. 5(a and c) as orthographic projections without perspective distortion. These images evidence a significant rearrangement involving the active material upon the first cycle. Such a notable change can in part justify the significant decrease in electrode/electrolyte interphase resistance and the cell improvement already observed by electrochemical tests in Figs. 2 and 3. In addition, the volume rendering after 100 cycles (Fig. 5e) reveals a substantial reduction of the overall sulfur phase into the electrode, which suggests either incomplete conversion of the long-chain polysulfides upon charging or electrodeposition at the

interface between electrode and separator [51]. Further insight into this reorganization is achieved by calculating for each dataset the sulfur phase fraction along the *Z* axis (Fig. 5b, d and f) which may approximately indicate the electrochemically active electrode depth. The related graph before cycling (Fig. 5b) shows the sulfur mostly distributed in the top surface of the electrode with an estimated depth of about 70 μm. After the first cycle (Fig. 5d) a large fraction of sulfur remains hosted in the top surface, while a significant part migrates within the electrode bulk likely due to electrodeposition into the porous structure of the current collector. The analysis of the electrode after 100 cycles (Fig. 5f) reveals a further migration of the sulfur to the inner side of the electrode film, thus further suggesting a remarkable role of the electrode bulk and the current collector in driving the electrochemical reaction of the Li/S cell, particularly upon prolonged cycling [51]. Therefore, both the heterogeneous composite electrode film and the porous current collector are expected to have complex interactions with the various lithium polysulfides [36,61]. Additional fundamental studies of such a multiphase process performed by EIS analyses on symmetrical Li-S cells might elucidate crucial aspects of the conversion reactions that are still poorly understood and reveal the diffusion properties of lithium polysulfides [62]. Despite being of definite interest, such an investigation of the Li-S process is beyond the scope of this work.

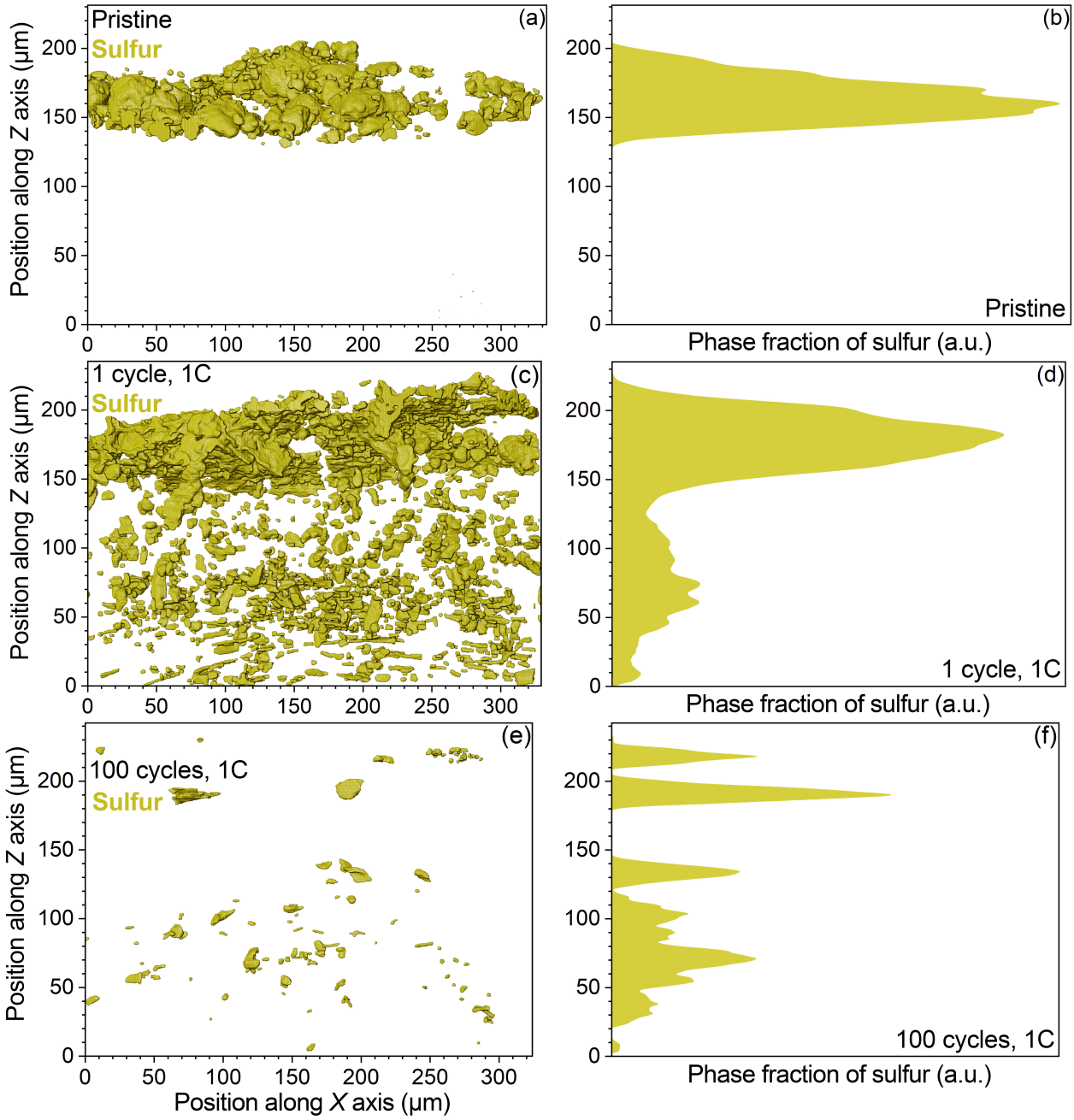

Fig. 5. Distribution of the sulfur phase in the S:Au 97:3 *w*/*w* electrodes with sulfur loading of 1.6–2.4 mg cm^{-2} (a and b) before and after (c and d) 1 and (e and f) 100 cycles at a 1C rate as determined by processing X-ray CT datasets. In detail: (a, c and e) volume rendering (orthographic projection) showing the distribution of the sulfur phase across the XZ plane, where X is the axis parallel to the electrode plane and *Z* is the sample rotation axis orthogonal to the electrode plane; (b, d and f) phase fraction of sulfur along the *Z* axis. Tomographic scans performed using a 40× lens and taking 1601 radiographs of the specimen through 360° with an exposure time of either 44 or 47 s for each projection and binning 1; voxel size: from 176 to 177 nm: field of view: ~330 µm. See Figs. 3 and 5 showing the cycling performance of the cell and the distribution of the sulfur phase in the electrode samples, respectively.

Further steps toward the achievement of practical Li-S batteries involve increasing the active material loading in the cathode and decreasing the E/S ratio in the cell [29,30,63]. Therefore, we investigate herein the S:Au 97:3 *w*/*w* material in a more challenging experimental condition using a coin-cell with sulfur loading of 5.7 mg cm^{-2} and E/S ratio of 5 μL mg_{Sulfur}^{-1}, still retaining a sulfur fraction of 78 wt% in the electrode film. Fig. 6 shows the voltage profiles (Fig. 6a) and cycling trend over 40 cycles (Fig. 6b) of the above Li|S:Au 97:3 *w*/*w* cell at the constant current rate of C/20, which correspond to about 0.5 mA cm^{-2}. Fig. 6(a) reveals that the increased loading, the limited electrolyte amount, and the notable sulfur ratio into the cathode, raise the polarization of the cell with respect to that using mild conditions reported in Fig. 3. On the other hand, the battery exhibits the typical voltage signature of the Li-S conversion process and displays a significant change of the curve after the 1st cycle (Fig. 6a). This above discussed process leads to an initial capacity increase from ca. 3.2 to 4.5 mAh cm^{-2} (referred to the electrode geometric area of 1.54 cm^2), subsequent fluctuations with a maximum value of 5.4 mAh cm^{-2} (i.e., about 950 mAh g_S^{-1}), and a final value of 4.2 mAh cm^{-2} (i.e., about 730 mAh g_S^{-1}) after 40 charge/discharge cycle (Fig. 6b).

We have systematically investigated elsewhere various sulfur-based composite electrodes [15,19,31,36,42,54,64] and optimized key cell parameters required for practical applications, such as the electrode loading and fraction of additives in the cathode [29,30,63]. A comparison of these data with the results of Fig. 6 may actually suggest viable approaches to overcome the challenges that presently hinder the transition of the Li-S technology from laboratory to the market. According to a widely used strategy, we have already employed carbon additives of various morphologies, such as multiwalled nanotubes [15,42], 3D frameworks [19,54,64], and amorphous nanometric powder [42], to prepare composite materials containing from 60 to 70 wt% of sulfur, corresponding to a loading in the electrode film ranging from 48 to 56 wt%. The use of multiwalled carbon nanotubes has allowed us to reach a maximum capacity of 5 mAh cm^{-2}, an active material loading of 4 mg_{Sulfur} cm^{-2}, and a S/additives ratio in the electrode film of 48:52 *w*/*w* [15]. This parameter has been increased to 56:44 *w*/*w* by reducing both the areal mass of sulfur to about 2.4 mg_{Sulfur} cm^{-2} and the maximum capacity

to about 3 mAh cm^{-2} [42]. Besides, 3D graphene-containing electrodes with 56 wt% sulfur have shown a maximum capacity ranging from 2 to 3 mAh cm^{-2}, with an areal loading of 2–3 mg_{Sulfur} cm^{-2} [19,54,64]. We have lately studied Sn-loaded electrode incorporating 64 wt% sulfur (S:Sn 80:20 *w*/*w*) which delivered a maximum capacity of 2 mAh cm^{-2} with a loading of 1.9 mg_{Sulfur} cm^{-2} [31]. In a subsequent work [36], the sulfur content and its areal loading in the electrode have been raised by including either Sn or Ni nanopowders (S:metal 85:15 *w*/*w*) to 68 wt% and 6.8 mg_{Sulfur} cm^{-2}, respectively, which was reflected as capacity values approaching 7 mAh cm^{-2}. Notably, this latter report [36] has shown that sulfur electrodeposits upon charging on the metal centers and within the porous current collector and forms micrometric particles smaller than those of pristine cathodes. In this regard, the S:Au 97:3 *w*/*w* electrode studied in this work exhibits similar microstructural changes when cycled in a lithium cell, and it provides a promising performance despite the notable decrease in weight fraction of additive, even in a very challenging condition, that is, with sulfur loading of 5.7 mg cm^{-2}, E/S ratio of 5 µL mg_{Sulfur}^{-1}, and sulfur fraction of 78 wt% into the electrode film. Such a low additive loading is reflected as a low volume fraction of Au in the electrode, in particular considering the high density of the noble metal when compared to sulfur, and might enable the achievement of critical metrics for possible cell application [30]. Bearing in mind the scale of electronic conductivity of bulk Sn, Ni, and Au, i.e., Sn < Ni < Au, and the straightforward proportional relation of additive loading, conductivity, and reversible capacity observed herein, we propose the S:Au 97:3 *w*/*w* material as promising electrode for lithium-sulfur batteries, in view of its electrochemical properties and expected gravimetric and volumetric energy density. On the other hand, the high cost of noble metals may represent a limit for practical applications of this cathode-engineering approach. However, we believe that our proof-of-concept work on the use of metal nanopowders in lithium-sulfur batteries as well as the achievement of a very limited ratio of the noble additive may certainly pave the way for future optimization of new cathode formulations with satisfactory performance and moderate cost.

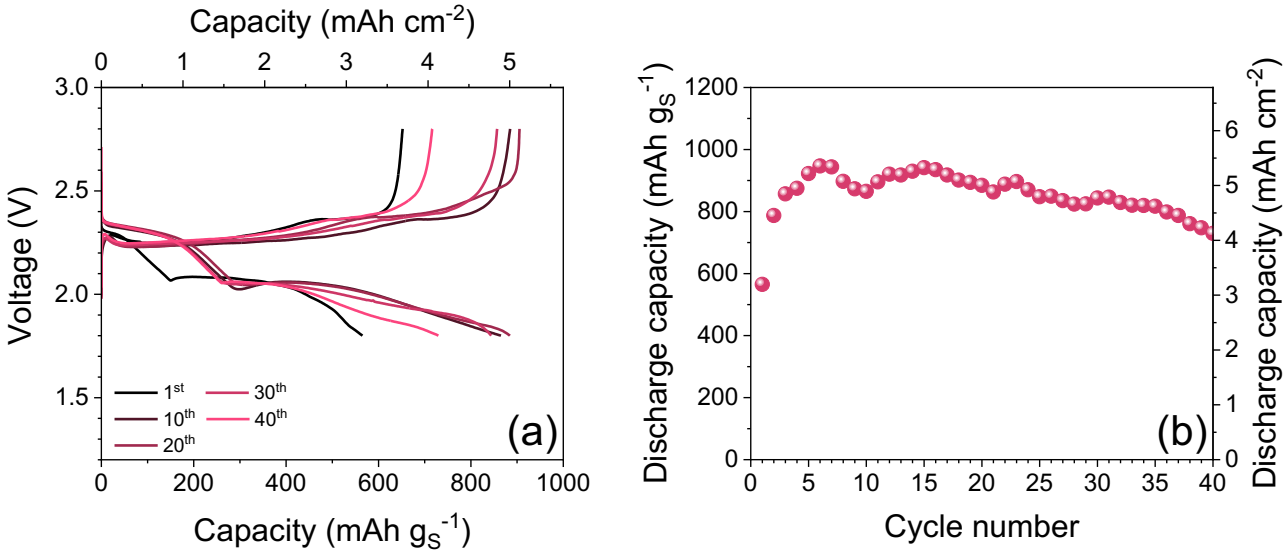

Fig. 6. (a) Voltage profiles and (b) cycling trend at the constant current rate of C/20 of the Li|S:Au 97:3 *w/w* cell with sulfur loading over the electrode of 5.7 mg cm^{-2} and E/S ratio of 5 µL mg_{Sulfur}^{-1} (1C = 1675 mA g_S^{-1}). Voltage range: 1.8–2.8 V. Electrode geometric area: 1.54 cm^2. Electrolyte: 1 mol kg^{-1} LiTFSI, 1 mol kg^{-1} $LiNO_3$ in DOL:DME 1:1 *w/w*. Temperature: 25 °C.

X-ray CT imaging in Fig. 7 demonstrates that increase in electrode loading and decrease in current rate only slightly affect the characteristic features of microstructural rearrangements associated with electrochemical activation of the cell upon a charge/discharge cycle. The figure shows cross-sectional slices visualized employing a grayscale (Fig. 7a and d) with corresponding segmentation (Fig. 7b and e) as well as segmented volume renderings of the samples in the field of view of the tomographic scan (Fig. 7c and f) referred to pristine and cycled electrodes. As discussed above, gold aggregates exhibit significant attenuation of the beam, thereby forming bright spots in Fig. 7(b and e). Instead, sulfur, carbon-cloth, and carbon-binder domain are visualized as gray regions of different brightness due to the significantly higher X-ray transmittance. The comparison between Fig. 7 and Fig. 4(a–f) with the same color map for visualization suggests similar depletion of sulfur along with its migration within the current collector pores by cycling. Furthermore, the low current rate and the increased loading likely boost the massive sulfur phase migration to the bulk, and limit its content into the electrode film. A thorough 3D representation of the electrodes is given by supplementary animations obtained by X-ray CT tomography (Movies S2).

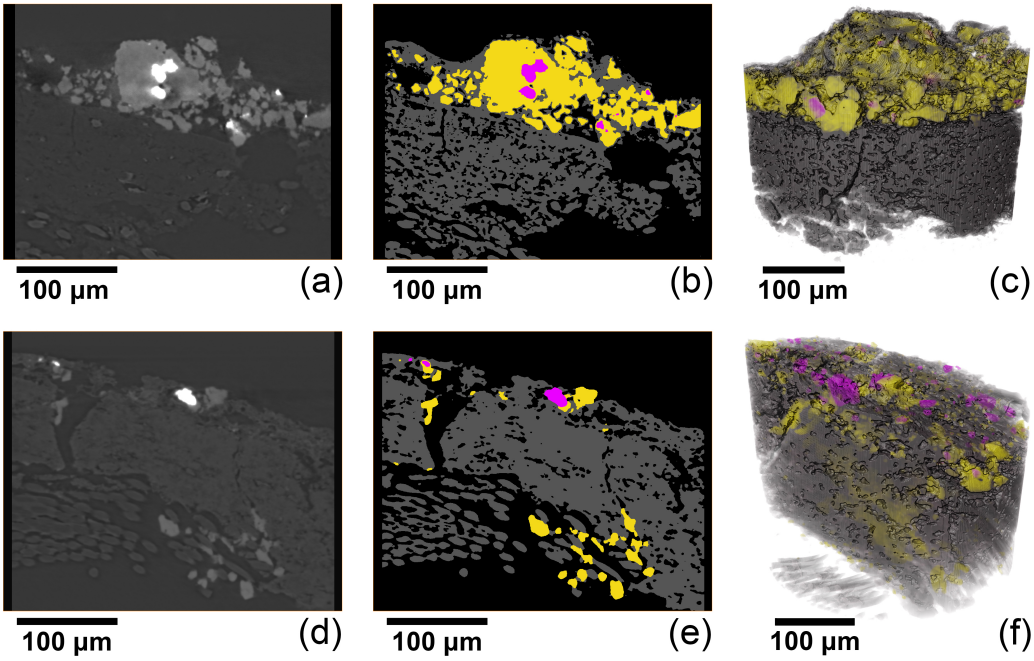

Fig. 7. X-ray CT imaging at the microscale of S:Au 97:3 *w*/*w* electrodes with sulfur loading of 4.1–4.2 mg cm^{-2} (a–c) before and after (d–f) 1 cycle at a C/10 rate. In detail: (a and d) cross-sectional slices extracted in a plane parallel to the rotation axis (*Z* axis) and orthogonal to the electrode plane (beam attenuation represented through a grayscale); (b and e) corresponding four-phase segmented slices (Au: magenta, S: yellow, C/PVDF/C-cloth: gray; exterior: black); (c and f) four-phase segmented volume rendering (Au: magenta, S: yellow, C/PVDF/C-cloth: gray; exterior: not represented). Tomographic scans performed using a 40× lens and taking 1601 radiographs of the specimen through 360° with an exposure time of either 44 or 46 s for each projection and binning 1; voxel size: 176 nm: field of view: ~330 µm. See Figs. 6 and 8 showing the cycling performance of the cell and the distribution of the sulfur phase in the electrode samples, respectively.

A more quantitative description of this process is provided in Fig. 8 which displays, in analogy to Fig. 5, the sulfur distribution for pristine (Fig. 8a and b) and cycled electrodes (Fig. 8c and d) in the field of view of the X-ray CT scan. Indeed, volume renderings (Fig. 8a and c) and phase fraction of sulfur as a function of the position along the sample rotation axis *Z* (Fig. 8b and d) are studied upon cycling. The pristine cathode film, having approximate thickness of 110 µm (Fig. 8a and b), is significantly depleted after 1 cycle due to a substantial migration of the sulfur phase toward the current collector bulk (Fig. 8c and d). Furthermore, the comparison with the results related to electrodes with

lower loading studied at higher current rate (Fig. 5) suggests a significant effect of the cycling conditions on the extent of sulfur relocation. Relevantly, Fig. 8(c and d) indicate a rather homogenous migration of the sulfur phase along the *Z* axis upon 1 cycle instead of the retention of large fraction on the electrode surface observed in Fig. 5(c and d), thus suggesting that current rate, electrode loading, and E/S ratio can drive the local kinetics of electrodeposition on the current collector. Therefore, we remark that the porous carbon support plays herein a crucial role in improving the cell performance during repeated charge/discharge cycles by providing suitable reaction sites for the reversible conversion of sulfur [24–26]. However, the replacement of the Al foils commonly used in battery as electrode support with thicker 3D current collectors having high surface area and containing large amount of carbon may possibly decrease both the volumetric and the gravimetric energy densities of the cell, thereby mitigating the enhancements by optimization of cathode film formulation. In this regard, both Figs. 4 and 7 reveal that a considerable fraction of electrode support has a negligible contribution to the electrochemical reaction, thereby suggesting large room for improvement by technological engineering of suitable 3D carbon frameworks. Indeed, *ad hoc* designed carbon-coated thin supports with similar microstructure and surface chemistry to those employed herein are expected to ensure comparable cycling performances and remarkable energy density.

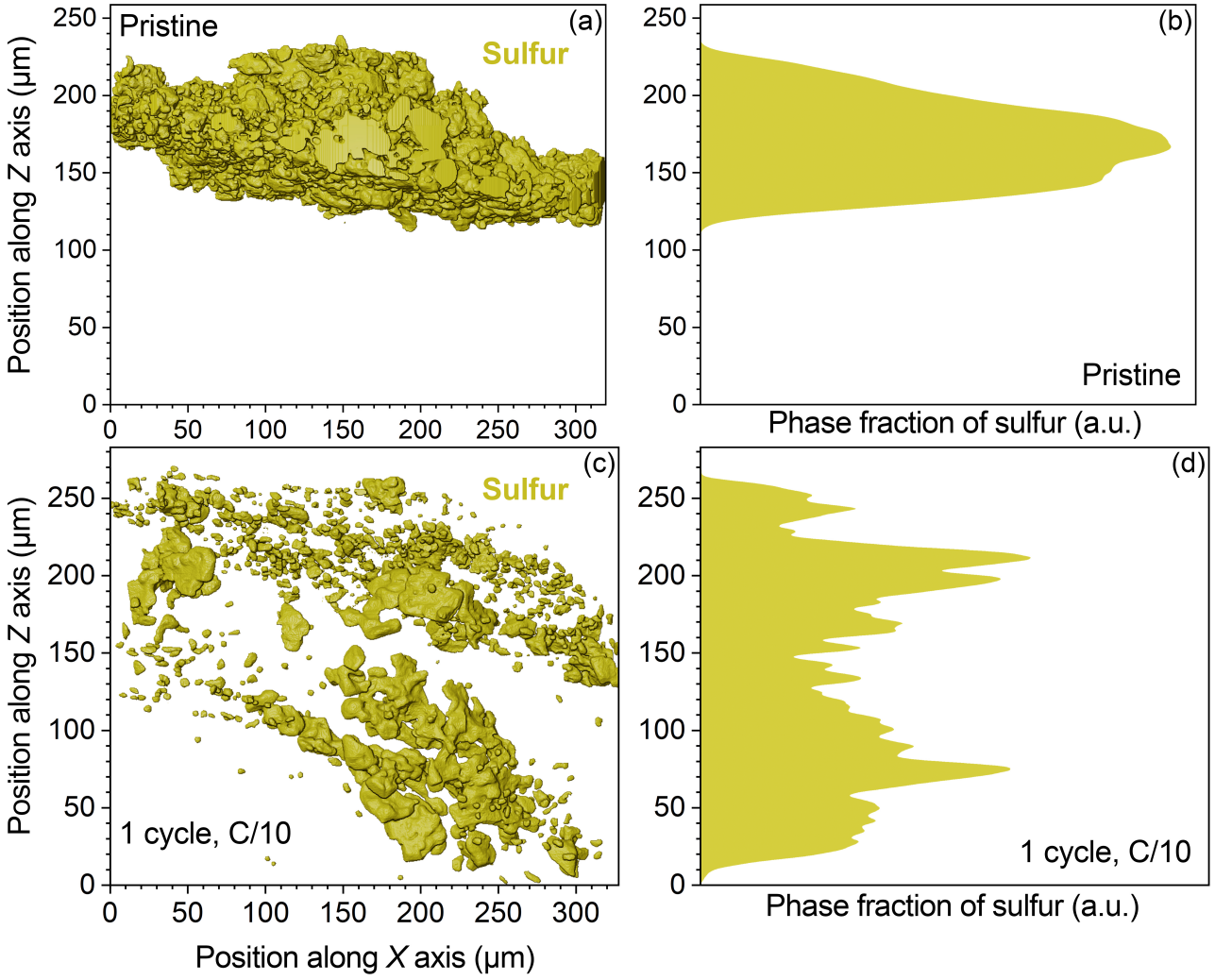

Fig. 8. Distribution of the sulfur phase in the S:Au 97:3 *w*/*w* electrodes with sulfur loading of 4.1–4.2 mg cm^{-2} (a and b) before and after (c and d) 1 cycle at a C/10 rate as determined by processing X-ray CT datasets. In detail: (a and c) volume rendering (orthographic projection) showing the distribution of the sulfur phase across the *XZ* plane, where *X* is the axis parallel to the electrode plane and *Z* is the sample rotation axis orthogonal to the electrode plane; (b and d) phase fraction of sulfur along the *Z* axis. Tomographic scans performed using a 40× lens and taking 1601 radiographs of the specimen through 360° with an exposure time of either 44 or 46 s for each projection and binning 1; voxel size: 176 nm: field of view: ~330 µm. See Figs. 6 and 8 showing the cycling performance of the cell and the distribution of the sulfur phase in the electrode samples, respectively.

The results on sulfur migration within the positive electrode reported herein are in full agreement with literature data [36,61] and reveal massive microstructural reorganizations in the cathode promoted by the reversible conversion of sulfur into soluble lithium polysulfides [65]. However, we have mentioned above that sulfur distribution in the pristine cathode affects the

electrochemical performance of the cell [42], and supposed that the pristine morphology might influence the microstructure of the carbon-binder domain and the sulfur nucleation sites upon charging, thus driving the reaction kinetics. In this regard, the S:Au 97:3 *w*/*w* electrode herein optimized may achieve an outstanding performance in a suitable cell configuration, as demonstrated in Fig. 9(a). Indeed, this composite cathode has been tested upon 300 cycles at a 2C rate in a lithium cell with a sulfur loading over the electrode of 1.4 mg cm^{-2} and an E/S ratio of 15 μL mg_{Sulfur}^{-1}, revealing a maximum capacity approaching 1300 mAh g_S^{-1} and a promising capacity retention at the end of the test of about 70%. These results further demonstrate the promising characteristics of the S:Au 97:3 *w*/*w* electrode formulation for application in lithium-sulfur batteries. Fig. 9(b and c) show the X-ray imaging of the anode before and after cycling, respectively, in terms of cross-sectional slices extracted in planes orthogonal to the electrode and volume rendering represented as an orthographic projection across the electrode plane. Similarly, Fig. S3 reports a 3D reconstruction by X-ray CT of the separator. Notably, the observed capacity fading is in part ascribable to undesired reactions occurring over the negative electrode and leading to precipitation of micrometric particles that possibly hinder a smooth lithium electrodeposition, rather than to an actual degradation of the cathode material, as indeed confirmed by *ex situ* X-ray CT analyses (Fig. 9b and c). Large precipitates are observed over the anode both before (Fig. 9b) and after cycling (Fig. 9c) as well as on the cycled separator (Fig. S3). The X-ray CT fully agrees with literature results [1] and reveals the formation of a native passivation layer (Fig. 9b) over the anode along with a massive precipitation of particles with heterogenous morphology upon prolonged cycling (Fig. 9c and Fig. S3). These precipitates have a higher density compared to lithium metal, which is reflected as different attenuation of the X-ray beam in Fig. 9(b and c). These results suggest additional improvements of the Li/S cell by developing *ad hoc* electrolyte formulations enabling *in situ* formation of a more stable SEI on the lithium-metal electrode and a smooth lithium electrodeposition, as well as by *ex situ* engineering of artificial passivation layers [10,64,66,67].

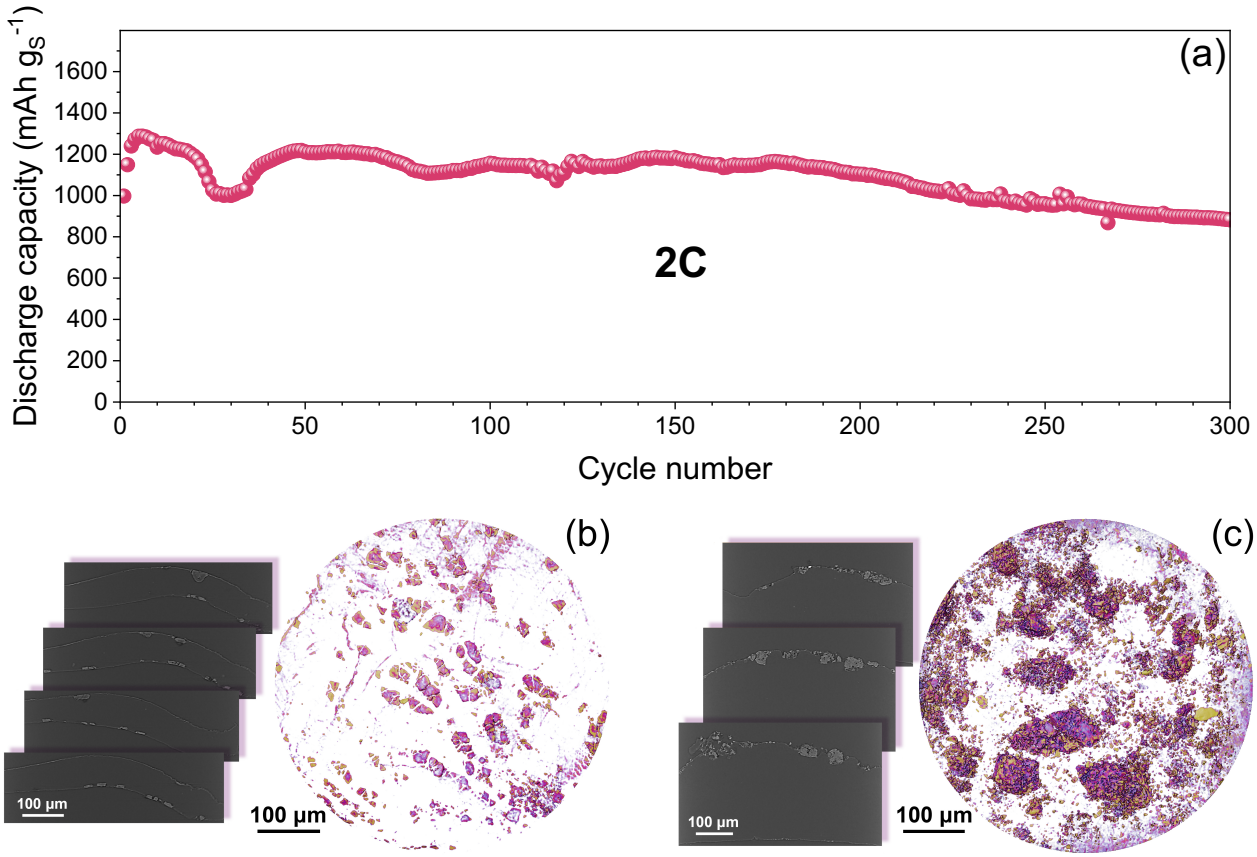

Fig. 9. (a) Discharge capacity of the Li|S:Au 97:3 *w*/*w* cell over 300 cycles at the constant current rate of 2C (1C = 1675 mA g_S^{-1}). The sulfur loading over the electrode is 1.4 mg cm^{-2} and the E/S ratio is 15 µL mg_{Sulfur}^{-1}. Voltage range: 1.8–2.8 V. (b and c) X-ray CT imaging at the microscale of the lithium-metal electrode (b) before and (c) after the cycling test, in terms of (left-hand side panels) cross-sectional slices extracted in planes orthogonal to the electrode and (right-hand side panels) volume rendering (orthographic projection) across the electrode plane; the sample of panel (b) was recovered from a Li|S:Au 97:3 *w*/*w* cell held at the OCV. Tomographic scans performed using a 20X lens and taking 901 radiographs of the specimen through 360° with an exposure time of 30 s for each projection and binning 1; voxel size: 301 nm: field of view: ~530 µm. See Fig. S3 for the X-ray CT imaging of the separator, as well as the Experimental section for details about sample preparation.

4. Conclusions

A gold-doped electrode has been investigated as positive electrode for high-energy lithium-sulfur battery. The active material has been straightforwardly achieved by mixing molten sulfur with gold nanopowder in the ratio of 97:3 *w*/*w*, and subsequent quenching at room temperature. X-ray CT reconstructions, electron microscopy images, and XRD patterns have revealed a crystalline composite in which the noble metal forms micrometric and sub-micrometric aggregates of nanometric primary particles smaller 100 nm surrounded by sulfur particles ranging from 5 to 50 μm. Therefore, we have prepared a cathode incorporating 78 wt% sulfur in the composite film by conventional casting of the active material on a carbon-cloth current collector. Notably, electrochemical characterization of the cathode in a lithium cell *via* voltammetry, impedance spectroscopy, and galvanostatic cycling has identified a significant change in sulfur conversion kinetics after the first discharge/charge cycle, reflected as remarkable decrease in electrode/electrolyte interphase resistance and increase in reversible capacity. X-ray CT analyses at the microscale have evidenced a relevant migration of sulfur phase upon cycling throughout the porous electrode from the surface to the inner side, and a gradual solubilization of the active material by prolonged cycling. Hence, the electrochemical activation of the cell during the initial cycles has been causally related to the microstructural reorganizations observed in the positive electrode. We have observed that the addition of gold in the cathode formulation causes an increase in both electronic and Li^+ conductivities within the electrode bulk, which triggers a raise in sulfur utilization and reversible capacity in lithium cell. Despite the low amount of additive in the cathode formulation, the lithium cell with sulfur loading of about 2 mg cm^{-2} and E/S ratio of 15 μL mg^{-1} has exhibited satisfactory rate capability, maximum capacity above 1300 mAh g_S^{-1} at C/10, capacities of about 1100 mAh g_S^{-1} at C/3 and 1000 mAh g_S^{-1} at 1C with retention in the 85%–91% range after 100 cycles, and coulombic efficiency approaching 100%. Cycling tests have shown that the sulfur loading in the positive electrode may be increased up to almost 6 mg cm^{-2} simultaneously decreasing the E/S ratio to 5 μL mg_{Sulfur}^{-1}, thereby reaching areal capacity values between 5.4 and 4.2 mAh cm^{-2}, which correspond to about 950 and 730 mAh g_S^{-1}, respectively. We

remark that the Li|S:Au 97:3 *w*/*w* cell has been able to achieve 300 cycles whilst retaining 70% of the maximum capacity. In this regard, X-ray CT has enabled us to clearly visualize large precipitates over the lithium-metal electrode, which possibly contribute to the partial degradation of the cell. Therefore, Au-doping and engineering of the porous electrode, along with optimization of a suitable electrolyte formulation, are suggested as viable strategies to attain the various cell metrics and performance figures for achieving a practical application of the Li-S battery.

Acknowledgements

This work was supported by the grant "Fondo di Ateneo per la Ricerca Locale (FAR) 2019", University of Ferrara, and performed within the collaboration project "Accordo di Collaborazione Quadro 2015" between University of Ferrara (Department of Chemical and Pharmaceutical Sciences) and Sapienza University of Rome (Department of Chemistry). The authors acknowledge funding from The Faraday Institution LiSTAR programme (EP/S003053/1, FIRG014). X-ray measurements were supported by funding from EPSRC (EP/K005030/1). PRS acknowledges the support of The Royal Academy of Engineering (CiET1718/59).

References

[1] L. Carbone, S.G. Greenbaum, J. Hassoun, Sustain. Energy Fuels. 1 (2017) 228–247.

[2] B. Scrosati, J. Garche, J. Power Sources. 195 (2010) 2419–2430.

[3] H.D. Yoo, E. Markevich, G. Salitra, D. Sharon, D. Aurbach, Mater. Today. 17 (2014) 110–121.

[4] L. Lu, X. Han, J. Li, J. Hua, M. Ouyang, J. Power Sources. 226 (2013) 272–288.

[5] D. Di Lecce, R. Verrelli, J. Hassoun, Green Chem. 19 (2017) 3442–3467.

[6] R. Fang, S. Zhao, Z. Sun, D.-W. Wang, H.-M. Cheng, F. Li, Adv. Mater. 29 (2017) 1606823.

[7] S. Chung, A. Manthiram, 31 (2019) 1901125.

[8] https://oxisenergy.com/products/.

[9] B. Scrosati, J. Hassoun, Y.-K.Y.-K. Sun, Energy Environ. Sci. 4 (2011) 3287.

[10] A. Varzi, K. Thanner, R. Scipioni, D. Di Lecce, J. Hassoun, S. Dörfler, H. Altheus, S. Kaskel, C. Prehal, S.A. Freunberger, J. Power Sources. 480 (2020) 228803.

[11] A. Manthiram, Y. Fu, S.-H.S.-H.S.-H. Chung, C. Zu, Y.-S. Su, Chem. Rev. 114 (2014) 11751–11787.

[12] C. Barchasz, F. Molton, C. Duboc, J.-C.J.-C. Leprêtre, S. Patoux, F. Alloin, Anal. Chem. 84 (2012) 3973–3980.

[13] J. Xiao, J.Z. Hu, H. Chen, M. Vijayakumar, J. Zheng, H. Pan, E.D. Walter, M. Hu, X. Deng, J. Feng, B.Y. Liaw, M. Gu, Z.D. Deng, D. Lu, S. Xu, C. Wang, J. Liu, Nano Lett. 15 (2015) 3309–3316.

[14] M.R. Busche, P. Adelhelm, H. Sommer, H. Schneider, K. Leitner, J. Janek, J. Power Sources. 259 (2014) 289–299.

[15] L. Carbone, T. Coneglian, M. Gobet, S. Munoz, M. Devany, S. Greenbaum, J. Hassoun, J. Power Sources. 377 (2018) 26–35.

[16] W. Li, Z. Liang, Z. Lu, H. Yao, Z.W. Seh, K. Yan, G. Zheng, Y. Cui, Adv. Energy Mater. 5 (2015) 1500211.

[17] N. Moreno, A. Caballero, L. Hernán, J. Morales, J. Canales-Vázquez, Phys. Chem. Chem. Phys. 16 (2014) 17332–17340.

[18] M. Sevilla, J. Carro-Rodríguez, N. Díez, A.B. Fuertes, Sci. Rep. 10 (2020) 4866.

[19] A. Benítez, D. Di Lecce, G.A. Elia, Á. Caballero, J. Morales, J. Hassoun, ChemSusChem. 11 (2018) 1512–1520.

[20] M. Li, W. Wahyudi, P. Kumar, F. Wu, X. Yang, H. Li, L.-J. Li, J. Ming, ACS Appl. Mater. Interfaces. 9 (2017) 8047–8054.

[21] Q. Pang, X. Liang, C.Y. Kwok, L.F. Nazar, Nat. Energy. 1 (2016) 16132.

[22] S.S. Zhang, Electrochim. Acta. 70 (2012) 344–348.

[23] M. Shaibani, M.S. Mirshekarloo, R. Singh, C.D. Easton, M.C.D. Cooray, N. Eshraghi, T. Abendroth, S. Dörfler, H. Althues, S. Kaskel, A.F. Hollenkamp, M.R. Hill, M. Majumder, Sci. Adv.

6 (2020) eaay2757.

[24] H.D. Shin, M. Agostini, I. Belharouak, J. Hassoun, Y.-K Sun, Carbon 96 (2016) 125–130.

[25] R. Fang, S. Zhao, P. Hou, M. Cheng, S. Wang, H.-M. Cheng, C. Liu, F. Li, Adv. Mater. 28 (2016) 3374–3382.

[26] A. Benítez, Á. Caballero, E. Rodríguez-Castellón, J. Morales, J. Hassoun, ChemistrySelect. 3 (2018) 10371–10377.

[27] H.-J. Peng, W.-T. Xu, L. Zhu, D.-W. Wang, J.-Q. Huang, X.-B. Cheng, Z. Yuan, F. Wei, Q. Zhang, Adv. Funct. Mater. 26 (2016) 6351–6358.

[28] D. Di Lecce, V. Marangon, A. Benítez, Á. Caballero, J. Morales, E. Rodríguez-Castellón, J. Hassoun, J. Power Sources. 412 (2019) 575–585.

[29] S. Dörfler, H. Althues, P. Härtel, T. Abendroth, B. Schumm, S. Kaskel, Joule. 4 (2020) 539–554.

[30] A. Bhargav, J. He, A. Gupta, A. Manthiram, Joule. 4 (2020) 285–291.

[31] V. Marangon, J. Hassoun, Energy Technol. 7 (2019) 1900081.

[32] J. He, A. Manthiram, Energy Storage Mater. 20 (2019) 55–70.

[33] F. Croce, A. D' Epifanio, J. Hassoun, A. Deptula, T. Olczac, B. Scrosati, 5 (2002) A47–A50.

[34] M. Jeong, S. Ahn, T. Yokoshima, H. Nara, T. Momma, T. Osaka, Nano Energy. 28 (2016) 51–62.

[35] Y.-C. Lu, H.A. Gasteiger, Y. Shao-Horn, J. Am. Chem. Soc. 133 (2011) 19048–19051.

[36] V. Marangon, D. Di Lecce, F. Orsatti, D.J.L. Brett, P.R. Shearing, J. Hassoun, Sustain. Energy Fuels. 4 (2020) 2907–2923.

[37] H. Al Salem, G. Babu, C. V. Rao, L.M.R. Arava, J. Am. Chem. Soc. 137 (2015) 11542–11545.

[38] C.-Y. Fan, P. Xiao, H.-H. Li, H.-F. Wang, L.-L. Zhang, H.-Z. Sun, X.-L. Wu, H.-M. Xie, J.-P. Zhang, ACS Appl. Mater. Interfaces. 7 (2015) 27959–27967.

[39] W. Zhang, C. Yang, B. Ding, J. Peng, F. Xu, M. Zheng, H. Hu, Y. Xiao, Y. Liu, Y. Liang, A self-crosslinking procedure to construct yolk–shell Au@microporous carbon nanospheres for

lithium–sulfur batteries, Chem. Commun. 56 (2020) 1215–1218. doi:10.1039/C9CC07625E.

[40] D. Di Lecce, S. Levchenko, F. Iacoviello, D.J.L. Brett, P.R. Shearing, J. Hassoun, X-ray Nano-computed Tomography of Electrochemical Conversion in Lithium-ion Battery, ChemSusChem. 12 (2019) 3550 – 3561. doi:10.1002/cssc.201901123.

[41] C. Tan, M.D.R. Kok, S.R. Daemi, D.J.L. Brett, P.R. Shearing, Three-dimensional image based modelling of transport parameters in lithium–sulfur batteries, Phys. Chem. Chem. Phys. 21 (2019) 4145–4154. doi:10.1039/C8CP04763D.

[42] D. Di Lecce, V. Marangon, W. Du, D.J.L. Brett, P.R. Shearing, J. Hassoun, The role of synthesis pathway on the microstructural characteristics of sulfur-carbon composites: X-ray imaging and electrochemistry in lithium battery, J. Power Sources. 472 (2020) 228424. doi:10.1016/j.jpowsour.2020.228424.

[43] B.A. Boukamp, A Nonlinear Least Squares Fit procedure for analysis of immittance data of electrochemical systems, Solid State Ionics. 20 (1986) 31–44. doi:10.1016/0167-2738(86)90031-7.

[44] B. Boukamp, A package for impedance/admittance data analysis, Solid State Ionics. 18–19 (1986) 136–140. doi:10.1016/0167-2738(86)90100-1.

[45] J.E.B. Randles, A cathode ray polarograph. Part II.—The current-voltage curves, Trans. Faraday Soc. 44 (1948) 327–338. doi:10.1039/TF9484400327.

[46] A. Ševčík, Oscillographic polarography with periodical triangular voltage, Collect. Czechoslov. Chem. Commun. 13 (1948) 349–377. doi:10.1135/cccc19480349.

[47] B. Hammer, J.K. Norskov, Why gold is the noblest of all the metals, Nature. 376 (1995) 238–240. doi:10.1038/376238a0.

[48] S. Waluś, C. Barchasz, R. Bouchet, J.-C. Leprêtre, J.-F. Colin, J.-F. Martin, E. Elkaïm, C. Baehtz, F. Alloin, Lithium/Sulfur Batteries Upon Cycling: Structural Modifications and Species Quantification by In Situ and Operando X-Ray Diffraction Spectroscopy, Adv. Energy Mater. 5 (2015) 1500165. doi:10.1002/aenm.201500165.

[49] S.-H. Yu, X. Huang, K. Schwarz, R. Huang, T.A. Arias, J.D. Brock, H.D. Abruña, Direct

visualization of sulfur cathodes: new insights into Li–S batteries via operando X-ray based methods, Energy Environ. Sci. 11 (2018) 202–210. doi:10.1039/C7EE02874A.

[50] S. Zhang, K. Ueno, K. Dokko, M. Watanabe, Recent Advances in Electrolytes for Lithium-Sulfur Batteries, Adv. Energy Mater. 5 (2015) 1500117. doi:10.1002/aenm.201500117.

[51] C. Tan, T.M.M. Heenan, R.F. Ziesche, S.R. Daemi, J. Hack, M. Maier, S. Marathe, C. Rau, D.J.L. Brett, P.R. Shearing, ACS Appl. Energy Mater. 1 (2018) 5090–5100.

[52] V. Marangon, Y. Tominaga, J. Hassoun, J. Power Sources. 449 (2020) 227508.

[53] A. Benitez, V. Marangon, C. Hernández-Rentero, Á. Caballero, J. Morales, J. Hassoun, Mater. Chem. Phys. (2020) 123484.

[54] A. Benítez, A. Caballero, J. Morales, J. Hassoun, E. Rodríguez-Castellón, J. Canales-Vázquez, Nano Res. 12 (2019) 759–766.

[55] A. Manthiram, S.-H. Chung, C. Zu, Adv. Mater. 27 (2015) 1980–2006.

[56] L. Carbone, J. Peng, M. Agostini, M. Gobet, M. Devany, B. Scrosati, S. Greenbaum, J. Hassoun, ChemElectroChem. 4 (2017) 209–215.

[57] A. Rosenman, R. Elazari, G. Salitra, E. Markevich, D. Aurbach, A. Garsuch, J. Electrochem. Soc. 162 (2015) A470–A473.

[58] W. Li, H. Yao, K. Yan, G. Zheng, Z. Liang, Y.-M. Chiang, Y. Cui, Nat. Commun. 6 (2015) 7436.

[59] R. Jayan, M.M. Islam, J. Phys. Chem. C. 124 (2020) 27323–27332.

[60] H. Ci, J. Cai, H. Ma, Z. Shi, G. Cui, M. Wang, J. Jin, N. Wei, C. Lu, W. Zhao, J. Sun, Z. Liu, ACS Nano. 14 (2020) 11929–11938.

[61] L. Zielke, C. Barchasz, S. Waluś, F. Alloin, J.-C. Leprêtre, A. Spettl, V. Schmidt, A. Hilger, I. Manke, J. Banhart, R. Zengerle, S. Thiele, Sci. Rep. 5 (2015) 10921.

[62] S. Drvarič Talian, J. Moškon, R. Dominko, M. Gaberšček, ACS Appl. Mater. Interfaces. 9 (2017) 29760–29770.

[63] D. Eroglu, K.R. Zavadil, K.G. Gallagher, J. Electrochem. Soc. 162 (2015) A982–A990.

[64] A. Benítez, D. Di Lecce, Á. Caballero, J. Morales, E. Rodríguez-Castellón, J. Hassoun, J. Power Sources. 397 (2018) 102–112.

[65] J. Robinson, K. Xi, R.V. Kumar, A.C. Ferrari, H. Au, M.-M. Titirici, A. Parra Puerto, A. Kucernak, S.D.S. Fitch, N. Garcia-Araez, Z. Brown, M. Pasta, L. Furness, A. Kibler, D. Walsh, L. Johnson, C. Holc, G. Newton, N.R. Champness, F. Markoulidis, C. Crean, R. Slade, E. Andritsos, Q. Cai, S. Babar, T. Zhang, C. (Tina) Lekakou, A. Rettie, N.N. Kulkarni, R. Jervis, M. Cornish, M. Marinescu, G. Offer, Z. Li, L. Bird, C. Grey, M. Chhowhalla, D. Di Lecce, T. Miller, D. Brett, R. Owen, S. Liatard, D. Ainsworth, P. Shearing, J. Phys. Energy. (2021) https://doi.org/10.1088/2515-7655/abdb9.

[66] M. Agostini, D.-J. Lee, B. Scrosati, Y.K. Sun, J. Hassoun, J. Power Sources. 265 (2014) 14–19.

[67] L. Carbone, M. Gobet, J. Peng, M. Devany, B. Scrosati, S. Greenbaum, J. Hassoun, ACS Appl. Mater. Interfaces. 7 (2015) 13859–13865.

Graphical abstract

Au-doping may enhance the Li-S battery cathode. This new formulation ensures 5.7 mg_{sulfur} cm^{-2}, an electrolyte loading of 5 µL mg_{sulfur}^{-1}, a capacity of 1300 mAh g_{sulfur}^{-1}, and a stable performance over 300 cycles.